Coordinated Adsorption/Desorption Kinetics Enabled by Surface Sulfur Decoration Over Mo_2C for Boosted Hydrogen Evolution Reaction

*Ting Guo, Hao Fei, Ruoqi Liu, Fangyang Liu, Dezhi Wang, and Zhuangzhi Wu**

Maintaining a consistently high current density growth rate in the hydrogen evolution reaction is highly challenging because the limited mass transfer rate at the electrode/electrolyte interface will make the adsorption reaction as the rate-determining step associated with a low hydrogen coverage, exhibiting a Tafel slope >120 mV dec^{-1}. Therefore, maximizing the current density range in which the desorption reaction is the rate-determining step, can significantly reduce the overpotential. Herein, a surface sulfur decoration strategy is presented to modify the molybdenum carbide electrocatalyst and achieve coordinated adsorption/desorption kinetics, leading to a dominant Volmer–Heyrovsky mechanism across a wide range of current densities. Both experimental and theoretical results validate the surface charge redistribution induced by sulfur decoration, which subtly optimizes the Gibbs free energy of hydrogen adsorption and enhances the in-plane polarization field. As a result, the as-obtained surface sulfur-decorated molybdenum carbide electrocatalyst exhibits coordinated adsorption/desorption kinetics and efficient hydrogen delivery, ultimately surpassing the commercial Pt/C electrocatalyst for high-efficiency hydrogen evolution.

1. Introduction

Hydrogen production by the electrocatalytic hydrogen evolution reaction (HER) is a dramatic electric energy conversion strategy and may convert surplus renewable electric energy (e.g., solar and wind power) into chemical energy in the format of hydrogen fuel (H_2) which can be stored, transported, and consumed at will without any pollutant.[1,2] However, maintaining a consistently high current density growth rate in HER is highly challenging, because as the overpotential increases, the adsorption reaction (i.e., Volmer reaction) will become the rate-determining step, while the mass transfer rate at the electrode/electrolyte interface is limited, leading to a very low hydrogen coverage on the electrocatalyst surface. At this time, the Tafel slope is >120 mV dec^{-1} and will continue to increase rapidly.[3] Therefore, maximizing the current density range in which the desorption reaction (i.e., Heyrovsky or Tafel reaction) is the rate-determining step can significantly reduce the overpotential, thereby saving electric energy consumption.

At this stage, platinum (Pt) and its alloy are the most effective electrocatalysts for HER due to the coordinated adsorption/desorption kinetics.[4,5] As shown in **Figure** 1a,b, Pt exhibits an ideal Gibbs free energy of hydrogen adsorption (ΔG_{H*}) value slightly less than zero at various hydrogen coverages, ensuring a sufficient supply of hydrogen intermediates and fast desorption reaction kinetics, thereby making desorption reaction the rate-determining step at the initial stage of HER. When the hydrogen coverage further increases to nearly 100%, the Tafel reaction becomes the rate-determining step, with an ultra-low Tafel slope of ≈30 mV dec^{-1}. The current density continues to increase rapidly until the limited mass transfer rate causes the adsorption reaction to become the rate-determining step once again, ultimately demonstrating that the desorption reaction maintains the rate-determining step over a wide range of current density. Nevertheless, the scarcity and high expense hinder the industrialization of Pt-based electrocatalysts for HER, and exploiting efficient non-noble-metal-based electrocatalysts is crucial for sustainable and scalable H_2 production.[6]

Molybdenum-based electrocatalysts, particularly molybdenum carbides are widely recognized as potential substitutes for Pt in the electrocatalytic HER.[7–17] However, the most active beta-molybdenum carbide (β-Mo_2C) typically exhibits a ΔG_{H*} value that is too negative, ranging from –0.67 to –0.31 eV at different coverages (Figure 1b), which benefits the adsorption of hydrogen intermediate but restricts the desorption step. This leads to uncoordinated adsorption/desorption kinetics, resulting in a narrow current density range where the desorption reaction dominates and a slow growth rate of current density, as shown in Figure S1a (Supporting Information). Fortunately, the ΔG_{H*} of Mo_2C can be effectively optimized through charge redistribution, as

---

T. Guo, H. Fei, R. Liu, D. Wang, Z. Wu
School of Materials Science and Engineering
Central South University
Changsha 410083, China
E-mail: zwu@csu.edu.cn

F. Liu
School of Metallurgy and Environment
Central South University
Changsha 410083, China

The ORCID identification number(s) for the author(s) of this article can be found under https://doi.org/10.1002/adfm.202407406

DOI: 10.1002/adfm.202407406

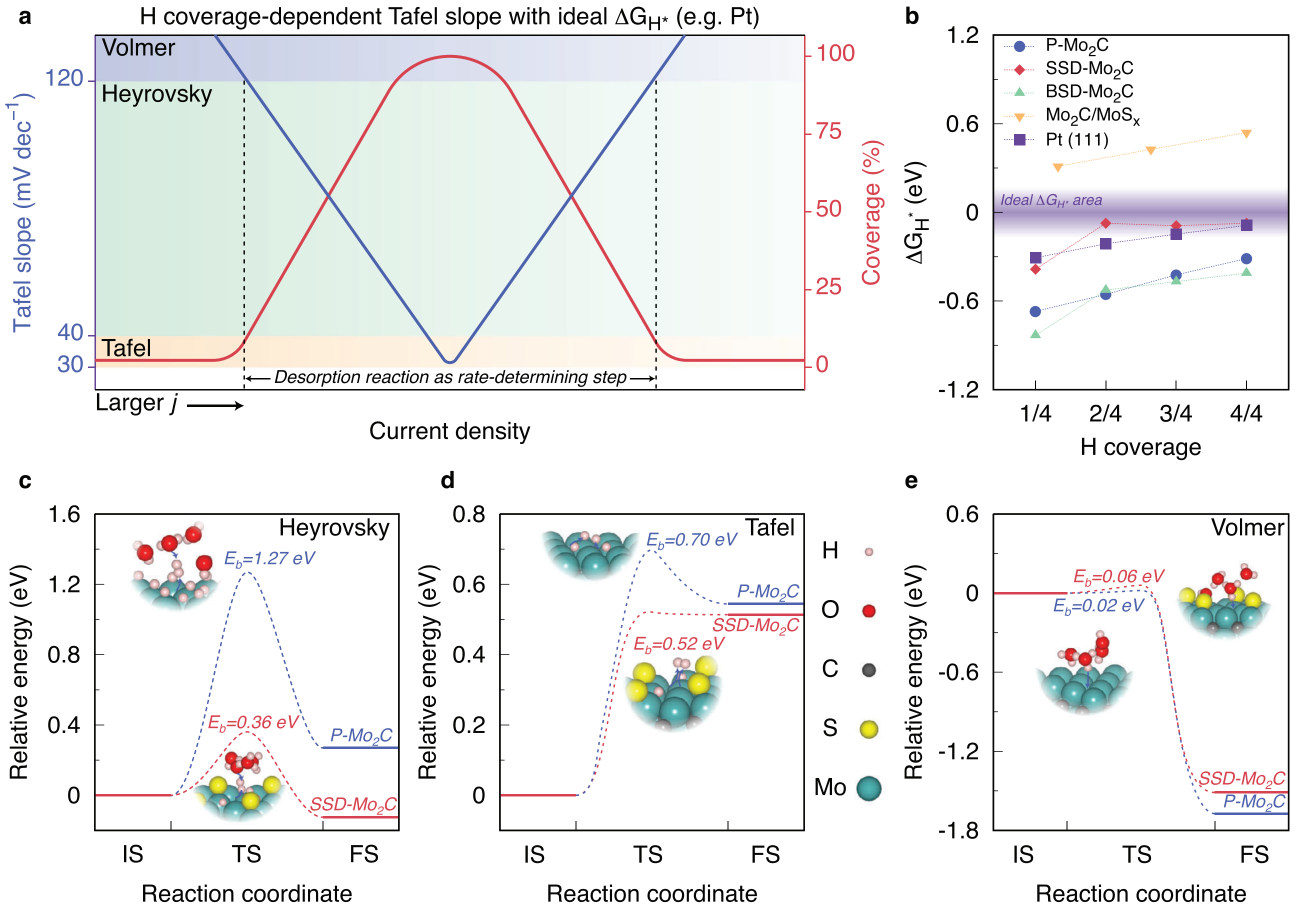

Figure 1. a) Schematic representation of H coverage-dependent Tafel slope with ideal ΔG_{H^*}. b) ΔG_{H^*} for various typical models at different H coverages. c–e) Relative energy diagram for Heyrovsky, Tafel, and Volmer reactions on P-Mo_2C and SSD-Mo_2C.

illustrated by several optimization strategies such as doping,[18] defect engineering,[19] and the construction of heterostructures.[20] Nevertheless, the primary focus of current research on Mo_2C-based HER electrocatalysts is still on weakening the Mo─H bond to optimize desorption kinetics, but the importance of coordinating adsorption/desorption kinetics is often ignored.

Relative to solely optimizing ΔG_{H^*}, utilizing the polarization field to construct a better hydrogen delivery mechanism is also an effective means of coordinating adsorption/desorption kinetics, as explored in several noble metal systems such as PtIr/CoP,[21] Pt/NiOOH,[22] MoO_xRh,[23] and Ru/Mo_2C.[24,25] Noble metals and substrates function as adsorption or desorption active sites, respectively, coupled with the polarization field established by charge redistribution, a rapid increase in current density over a prolonged period is achieved. However, the polarization field effect in non-noble electrocatalysts has been overlooked.

In stark contrast to Mo_2C, as shown in Figure S1b (Supporting Information), molybdenum sulfide (MoS_2) exhibits a too positive ΔG_{H^*} value,[26–28] which leads to fast desorption kinetics but insufficient hydrogen coverage. It is reasonable to coordinate the adsorption/desorption kinetics of Mo_2C through charge redistribution induced by sulfur (S) atoms. Inspired by the aforementioned insights, this work proposes a surface sulfur decoration strategy to regulate the surface electronic structure of Mo_2C, optimizing desorption kinetics and hydrogen delivery mechanisms. Both experimental and theoretical results validate the surface charge redistribution, which subtly optimizes the ΔG_{H^*} and enhances in-plane polarization fields, leading to coordinated adsorption/desorption kinetics and efficient hydrogen delivery, which ultimately surpasses the commercial Pt/C electrocatalyst for high-efficiency hydrogen evolution.

2. Results and Discussion

The feasibility of S atoms modifying the Mo_2C electrocatalyst to coordinate the adsorption/desorption kinetics is verified by density functional theory (DFT) calculations first. Figure 1b displays the ΔG_{H^*} at different hydrogen coverages of three typical S/Mo_2C systems, namely SSD-Mo_2C (surface sulfur-decorated molybdenum carbide), BSD-Mo_2C (bulk sulfur-doped molybdenum carbide), and Mo_2C/MoS_x heterostructure. Additionally, the data for P-Mo_2C (pristine molybdenum carbide) and Pt (111) are provided as references. (Detailed model structures and DFT calculations are provided in the Supporting Information). P-Mo_2C exhibits a ΔG_{H^*} ranging from –0.67 to –0.31 eV at different coverages, indicating that the adsorption process of hydrogen intermediates is facile. However, the desorption process is hindered, leading to the accumulation of hydrogen intermediates on the electrocatalyst surface during the initial stages of the HER, both adsorption and desorption reactions are very slow, resulting in a low current density growth rate. For BSD-Mo_2C, the ΔG_{H^*} is almost identical to that of P-Mo_2C, indicating that bulk sulfur doping has minimal effect on the surface charge distribution of Mo_2C which may be attributed to the fact that the electronegativity of sulfur (2.58) is very close to that of carbon (2.55). Mo_2C/MoS_x demonstrates a much better optimization effect, with ΔG_{H^*} ranging from 0.23 to 0.33 eV. Both adsorption and desorption reactions can proceed relatively faster at a relatively high overpotential. However, the corresponding HER onset overpotentials will also be high, as observed in the previous research.[29] Inspiringly, SSD-Mo_2C exhibits a variation trend of ΔG_{H^*} similar to that of Pt (111). The ΔG_{H^*} of –0.38 eV at lower coverages will be highly beneficial to the supply of hydrogen intermediates in the initial stage of HER. As the hydrogen coverage gradually increases, the ΔG_{H^*} approaches zero and is completely comparable to Pt (111), indicating that the sulfur decoration can effectively coordinate the adsorption/desorption kinetics.

To further investigate the HER kinetics of SSD-Mo_2C, transition state calculations were also conducted, as shown in Figure 1c–e. SSD-Mo_2C exhibits much lower energy barriers than P-Mo_2C for both Heyrovsky and Tafel mechanisms, which evidences the optimized desorption kinetics. At the same time, there is only a negligible increase (0.04 eV) in the energy barriers of the Volmer mechanism for SSD-Mo_2C, thus preserving the benefits of adsorption of hydrogen intermediates derived from Mo_2C. The preferable HER reaction kinetics of SSD-Mo_2C indicate the potential for coordinating adsorption/desorption kinetics with a high current density growth rate over a prolonged range.

Guided by the predictions from DFT calculations, the SSD-Mo_2C electrocatalyst was synthesized by a sacrificial template method, as illustrated in **Figure 2a**. The in situ sulfurized Cu_2O nanocubes (Cu_2O@CuS) served as both a sulfur source and template, the polydopamine (PDA) was a reduction agent and carbon source. During the high-temperature carbonization process, the surface of Mo_2C was decorated by the side H_2S gas. The Cu_2O@CuS template was reduced to inert copper nanoparticles and finally eliminated through Fe^{3+} etching treatment. Throughout the entire synthesis process, the nanocubic structure has been well inherited in SSD-Mo_2C products, with a uniform distribution of Mo, C, and S elements, as illustrated in Figure S9 (Supporting Information). Additionally, Figure S10 (Supporting Information) shows the X-ray diffraction (XRD) patterns and X-ray photoelectron spectroscopy (XPS) spectra of various intermediate products, confirming the presence of S species in Cu_2O@CuS, as well as the complete elimination of all Cu species after Fe^{3+} etching. Finally, the atomic ratio of Mo/S in SSD-Mo_2C was estimated as 6.9 based on the wide-scan survey XPS spectrum.

The XRD patterns of SSD-Mo_2C and P-Mo_2C are shown in Figure 2b, and all the diffraction peaks are consistent with the hexagonal β-Mo_2C (P63/mmc, JCPDS 35–0787),[30,31] implying that the H_2S gas is insufficient to synthesize fine MoS_2 crystal, but decorates S atoms on the surface of β-Mo_2C merely. To investigate the surface electronic structure changes of Mo_2C after surface sulfur decoration, XPS and ultraviolet photoelectron spectroscopy (UPS) were performed. The high-resolution Mo 3d spectra are depicted in Figure 2c, and the signals located at 228.6 and 231.8 eV should be assigned to the Mo^{2+} species relevant to Mo—C bond.[7,32,33] The well-retained Mo—C bond of SSD-Mo_2C demonstrates the S decoration on β-Mo_2C surface rather than inserting into lattice, in agreement with the XRD analysis. The Mo^{4+} and Mo^{6+} species are related to the characteristic of Mo—O bonds over MoO_2 and MoO_3, respectively,[19,34] which are commonly observed in transition-metal carbide-based materials on account of surface oxidation.[14] The most significant difference is the new emerging peaks between Mo^{2+} and Mo^{4+} species, named the C–Mo–S linker in this work, which can be attributed to the charge transfer from Mo to S or C atoms induced by S decoration, leading to a shift of partial Mo^{2+} species to higher binding energy. Simultaneously, the C 1s spectra (Figure 2d) exhibit a shift of the C—Mo bond toward lower binding energy, in agreement with the results of Mo 3d spectra. Similar conclusion can also be inferred from the UPS spectra (Figure S11a, Supporting Information), in which SSD-Mo_2C exhibits a larger work function (Φ) than P-Mo_2C, indicating that the electrons from Mo_2C surface prefer to transfer to the decorated S atoms.[25] Additionally, the surface charge density was evaluated by measuring the Zeta potential.[35] As shown in Figure S11b (Supporting Information), after surface sulfur decoration, the average Zeta potential increased from –21.67 to –27.12 mV, indicating the increased charge density due to surface charge redistribution. To further elucidate the interaction between S atoms and Mo_2C, we conducted electron paramagnetic resonance (EPR) analysis. As shown in Figure 2e, a signal at $g = 2.003$, corresponding to a non-metallic radical species, was observed in SSD-Mo_2C. This signal is similarly observed in molecular-based coordination polymer amorphous molybdenum sulfide.[36] In summary, we believe that the S atoms in SSD-Mo_2C interact with the terminal Mo atoms of Mo_2C, existing in a form similar to the non-metallic radical species found in amorphous molybdenum sulfide. These differences in surface properties demonstrate that the surface electronic structures of Mo_2C can be regulated by S decoration, ultimately having a significant influence on the adsorption/desorption kinetics in the HER.

To further explore the structure and morphology of SSD-Mo_2C, transmission electron microscope (TEM) characterization was performed, as shown in Figure 2f,g. The size of a single SSD-Mo_2C hollow nanocube is ≈800 nanometers, with a wall thickness of ≈25–50 nanometers. The hollow structure not only provides sufficient exposed active sites to be occupied by S atoms and utilized for efficient HER, but also promotes mass transfer, further increasing the current density growth rate. High resolution TEM (HR-TEM) image shows an interplanar spacing of 0.26 nm, which is attributed to the (100) plane of hexagonal β-Mo_2C, consistent with the XRD results. The corresponding atomic model representing the (001) plane of hexagonal β-Mo_2C is inserted in the image. Based on the DFT calculation results, the hollow site consisting of three Mo atoms on the (001) plane is preferable for the occupation of S atoms. Therefore, larger light spots within the same hollow site in the HR-TEM image may be attributed to the decoration of S atoms.[37]

To validate the optimization of surface sulfur decoration for Mo_2C in HER kinetics, the electrochemical HER performance of SSD-Mo_2C and P-Mo_2C was studied. The linear sweep voltammetry (LSV) with Pt/C as a benchmark, as depicted in **Figure 3a**

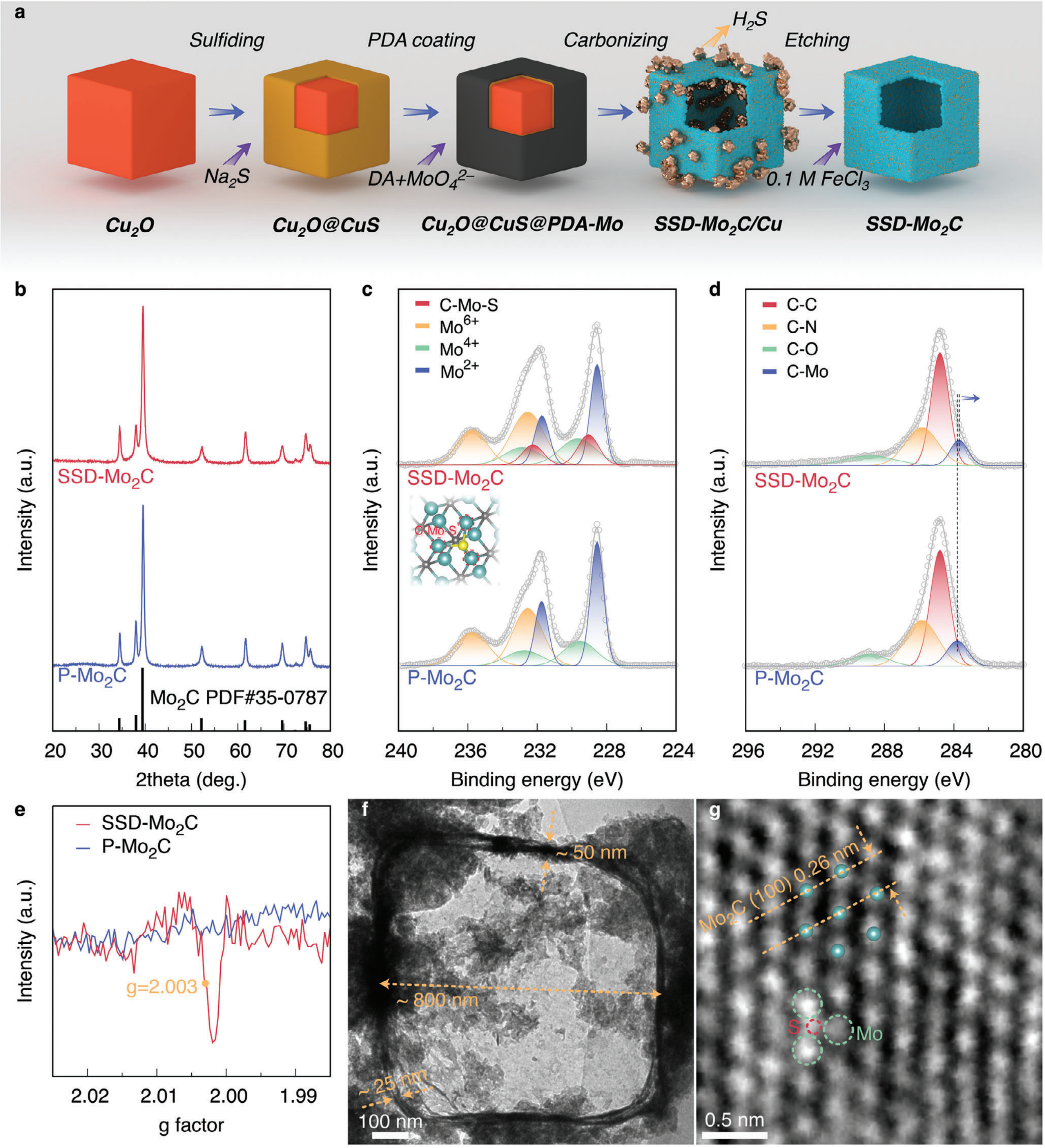

Figure 2. a) Schematic illustration for the synthesis process of SSD-Mo_2C. XRD patterns; b), Mo 3d XPS spectra; c), C 1s XPS spectra d), and EPR spectra; e) of SSD-Mo_2C and P-Mo_2C. f,g) TEM and HR-TEM images of SSD-Mo_2C.

and P-Mo_2C requires 181 mV to reach a current density of 10 mA cm^{-2} (η_{10}), which is consistent with previous reports.[13] After surface sulfur decoration, SSD-Mo_2C exhibits a smaller η_{10} of 130 mV as well as a remarkably faster current density growth rate, even surpassing Pt/C after 332 mV. A clearer variation trend of current density growth rate can be observed from the Tafel slope (Figure 3b). SSD-Mo_2C exhibits a significantly lower Tafel slope of 50 mV dec^{-1} compared to P-Mo_2C, implying that the Heyrovsky reaction is the rate-determining step, consistent with the results of most Mo_2C-based electrocatalysts.[38–41] Although the

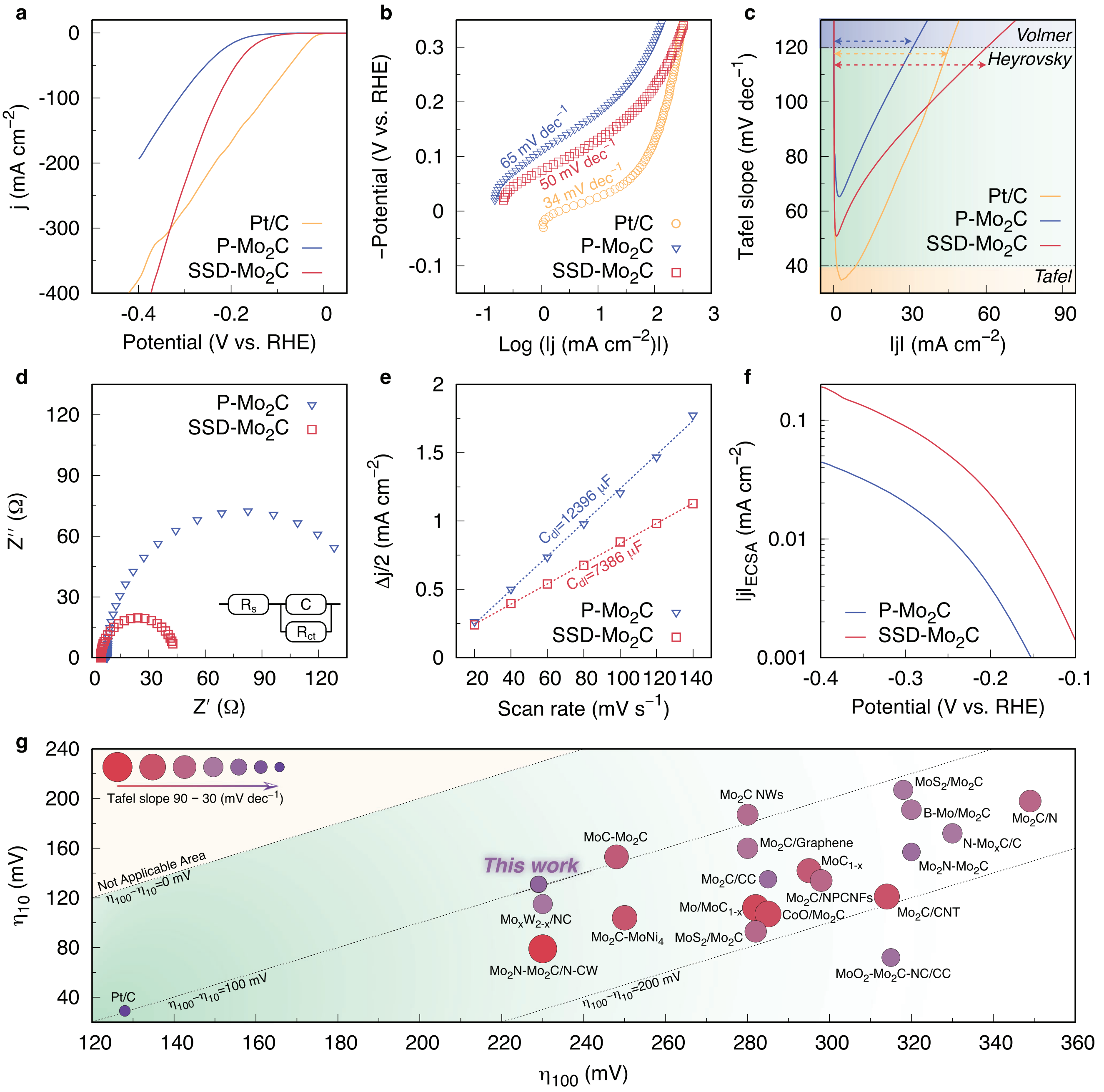

Figure 3. Electrochemical HER performances of SSD-Mo$_2$C and P-Mo$_2$C. a) Polarization curves. b) Tafel slope plots. c) Plots of current density versus Tafel slope. d) Nyquist plots. e) Plots of capacitive currents versus scan rate. f) Polarization curves normalized by ECSA. g) Comparison of SSD-Mo$_2$C with other reported Mo$_2$C-based electrocatalysts.

lowest Tafel slope value is higher than that of Pt/C, SSD-Mo$_2$C maintains a Tafel slope of 50–120 mV dec^{-1} with the dominant Volmer–Heyrovsky mechanism across a larger current density range until 60 mA cm^{-2}, as shown in Figure 3c. In contrast, the current density range for the Volmer–Heyrovsky mechanism of P-Mo$_2$C is only 31 mA cm^{-2}, indicating that surface sulfur decoration can effectively enlarge the current density range in which the desorption reaction is the rate-determining step due to coordinated adsorption/desorption kinetics.

Electrochemical impedance spectroscopy was carried out to further probe the charge-transfer properties during the HER process. Figure 3d displays the Nyquist plots fitted with the corresponding equivalent circuit as shown in the inset. SSD-Mo$_2$C exhibits much lower charge transfer resistance values (39.3 Ω) than that of P-Mo$_2$C (144.9 Ω), suggesting faster adsorption/desorption kinetics in HER process, in accordance with the Tafel slope plots. Moreover, the electrochemically active surface area (ECSA) of SSD-Mo$_2$C and P-Mo$_2$C samples were estimated via the electrochemical double-layer capacitance (C_{dl}) (detail calculation given in the Supporting Information). As displayed in Figure 3e, evident decrease can be observed over the C_{dl} values of SSD-Mo_2C comparing with P-Mo_2C, which should be attributed to the occupation of S atoms, reducing partial available active sites for hydrogen. Therefore, the Cu_2O@CuS templates with different sulfurization time were used to further optimize the electrocatalytic activity. Figure S12 (Supporting Information) depicts the plots of LSV, Tafel slope, and capacitive currents versus scan rate of SSD-Mo_2C employing various Cu_2O@CuS templates. And with the increase of sulfurization time, the HER performance initially improves significantly, followed by a subsequent decline. The optimal sulfurization time is found to be 120 s, indicating that appropriate surface sulfur decoration can achieve the optimal balance between active sites and reaction kinetics. Despite the degradation in active sites triggered by surface sulfur decoration, the overall HER performance of Mo_2C has been significantly enhanced, indicating that the decorated S atoms improve the intrinsic catalytic activity of Mo_2C by inducing charge redistribution. The polarization curves normalized by ECSA further confirm this conclusion, as shown in Figure 3f, in which SSD-Mo_2C consistently exceeds P-Mo_2C by several orders of magnitude in ECSA-fitted current density. The electrochemical performance characterizations demonstrate the superiority of surface sulfur decoration in optimizing the HER kinetics of Mo_2C, as further evidenced by the comparison with reported Mo_2C-based electrocatalysts in Figure 3g. From a practical perspective, the HER electrocatalysts are evaluated by the required overpotential to achieve a particular current density, i.e., η_{10}, which is ultimately decided by both the initial potential and Tafel slope. Hence, we compared the η_{10}, η_{100}, and Tafel values of the reported Mo_2C-based electrocatalysts, SSD-Mo_2C, and Pt/C in a single graph. Some interesting phenomena can be observed, and most of the HER electrocatalysts require an overpotential ranging from ≈100–200 mV to increase the current density from 10 to 100 mA cm^{-2}, even for Pt/C with an ultra-low Tafel slope of 34 mV dec^{-1}, also requiring 99 mV. The main reason is that with the increase of current density, the limited mass transfer rate at the electrode/electrolyte interface leads to the adsorption reaction becoming the rate-determining step, as well as low hydrogen coverage, resulting in slow HER kinetics.[3] In this work, coordinated adsorption/desorption kinetics achieved by surface sulfur decoration enable SSD-Mo_2C to maintain the desorption reaction as the rate-determining step over a wide current density range, significantly reducing the required overpotential to increase the current density from 10 to 100 mA cm^{-2} to be 98 mV, which is comparable to Pt/C and surpasses most reported Mo_2C-based electrocatalysts.

Stability is also crucial for evaluating electrocatalysts. As depicted in Figure S13a (Supporting Information), the polarization curve of SSD-Mo_2C shows a negligible decay merely after 2000 cyclic voltammetry cycles. With regard to chronoamperometry test (Figure S13b, Supporting Information), after testing for 30 h at 100 mA cm^{-2}, the current density remained above 85%, indicating a good durability over SSD-Mo_2C. Additionally, the XRD pattern, SEM image, S 2p XPS spectrum, and Raman spectrum after the stability test demonstrate the stable structure and composition of Mo_2C and confirm the good stability of S species in SSD-Mo_2C (Figure S13c–e, Supporting Information).

To further clarify the optimization mechanism of surface sulfur decoration comprehensively, additional experiments and DFT calculations were also conducted. First, two other typical configurations of sulfur-modified Mo_2C electrocatalysts as discussed in Figure 1b, BSD-Mo_2C and Mo_2C-MoS_x were synthesized and characterized. The XRD patterns of all samples are compared in Figure S14a (Supporting Information), no obvious differences can be observed, and all the diffraction peaks match well with the hexagonal β-Mo_2C standard card (P63/mmc, JCPDS 35–0787). Figure S14b,c (Supporting Information) further reveals the surface chemical states under various sulfur modification conditions. The XPS Mo 3d spectra of BSD-Mo_2C are nearly the same as P-Mo_2C, which can be attributed to the similar electronegativity of S and C, as discussed in Figure 1b. The S 2p spectra show that S atoms only exist as low-binding energy bulk S^{2-}, indicating that most S atoms are within the lattice rather than on the surface of Mo_2C. After hydrothermal sulfuration, the signals of Mo^{6+} species disappear entirely in Mo_2C-MoS_x, which should be attributed to the sulfurization of MoO_3 species during hydrothermal reaction as well as the excellent oxygen resistance ability from MoS_x shell on the surface.[42] By contrast, the signals of Mo^{4+} species are enhanced after hydrothermal sulfuration. At the same time, two new peaks at 230.6 and 233.8 eV are detected, indicating the existence of Mo^{5+} oxidation state.[32,43] The emergence of Mo^{4+} and Mo^{5+} species should be attributed to amorphous MoS_x, as indicated by the dominant typical signals of bridging $S_2{}^{2-}$ or apical S^{2-} with higher binding energies in the S 2p spectra.[44] SSD-Mo_2C exhibits similar signals with higher binding energies, which is consistent with the EPR results. Based on the crystalline structure of Mo_2C, the signals with higher binding energies should be mainly ascribed to the apical S^{2-} occupying the hollow sites of Mo_2C surface.

Based on the above discussion, different configurations of sulfur-modified Mo_2C electrocatalysts exhibit distinctly different surface chemical states, which will significantly impact the catalytic activity in HER, as depicted in Figure S15 (Supporting Information). BSD-Mo_2C exhibits a slightly higher current density, but there is no significant improvement in HER kinetics. The current density range for the Volmer-Heyrovsky mechanism is almost the same as that of P-Mo_2C. The minor performance improvement may be derived from the boosted charge transfer ability of the electrocatalyst due to heteroatoms doping.[10] Therefore, the effective S species for coordinating adsorption/desorption kinetics in this work should be those with higher binding energies, which account for 40% in SSD-Mo_2C according to S 2p spectra. Mo_2C-MoS_x shows relatively faster HER kinetics with a lower Tafel slope of 48 mV dec^{-1} as well as dominant Volmer-Heyrovsky mechanism over a longer period than P-Mo_2C. However, the poor charge transfer capacity and serious loss of active sites lead to unsatisfactory overall HER performance for Mo_2C-MoS_x. In conclusion, the superiority of surface sulfur decoration in optimizing the HER performance of Mo_2C is further confirmed by comparing different configurations of sulfur-modified Mo_2C electrocatalysts.

The different surface chemical states observed in various configurations of sulfur-modified Mo_2C imply distinct catalytic activities and electronic structures. According to the d-band center (ε_d) theory, the ε_d exhibits a strong correlation with the adsorption characteristics of electrocatalysts toward reaction

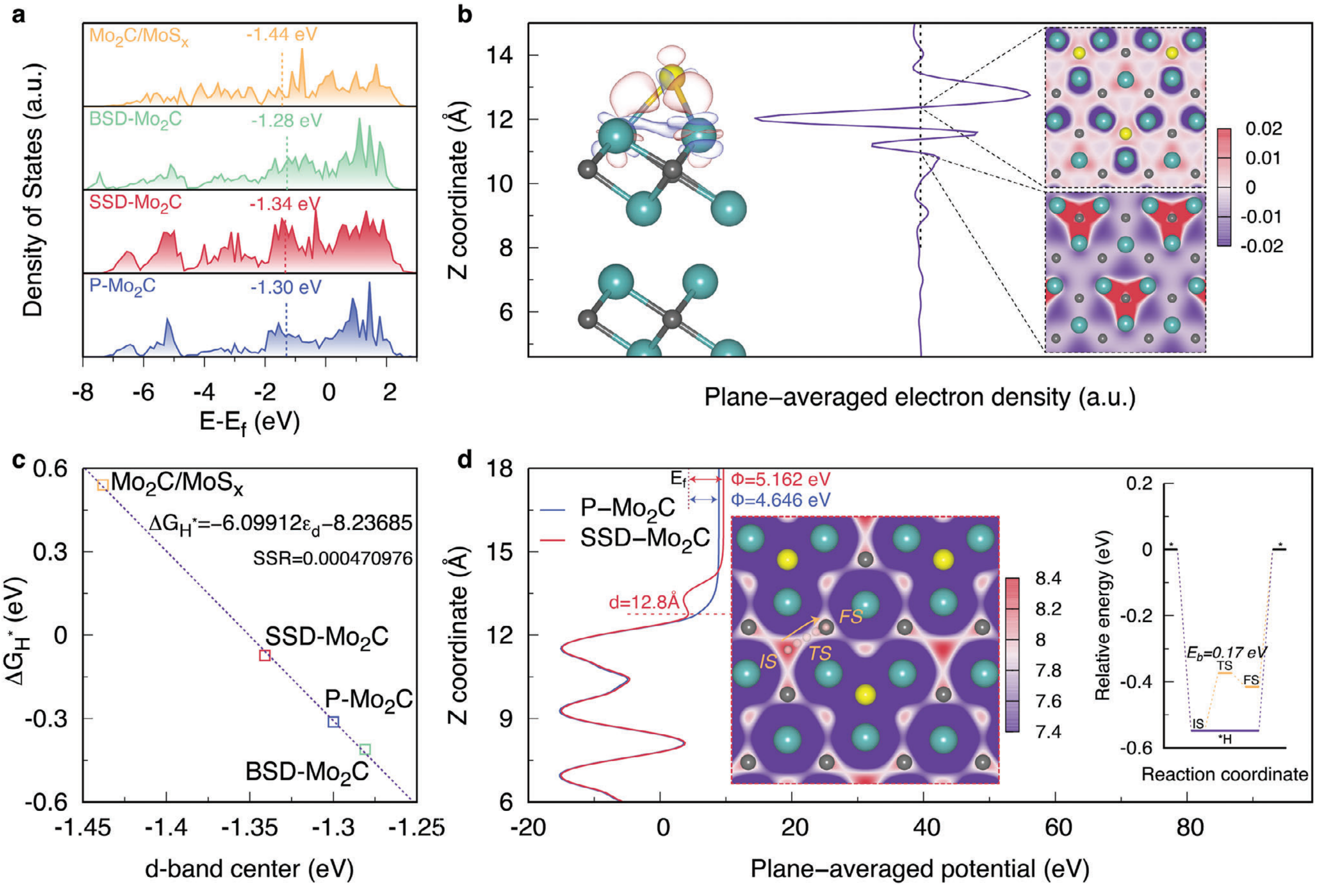

Figure 4. a) pDOS of the d-band and relative ε_d of P-Mo_2C, SSD-Mo_2C, BSD-Mo_2C, and Mo_2C/MoS_x. b) Charge density difference and the corresponding plane-average profile after sulfur decoration, the red and blue contours represent charge accumulation and dilution, respectively. c) Linear relationship between ε_d and ΔG_{H*}. d) Plane-averaged potential of P-Mo_2C and SSD-Mo_2C along the Z-coordinate and illustration of the hydrogen diffusion pathway under the influence of in-plane polarization field.

intermediates,[45] i.e., hydrogen adsorption in HER. **Figure 4a** displays the projected density of states (pDOS) of the d-band, and a shift down of the ε_d can be observed in SSD-Mo_2C, which weakens the Mo—H binding, consistent with the ΔG_{H*} calculation results. A minor uplift of the d-band center for BSD-Mo_2C and a noticeable downshift for Mo_2C-MoS_x are also observed. Furthermore, a well-fitted linear relationship between ε_d and ΔG_{H*} is plotted in Figure 4c, indicating that ε_d can serve as an ideal descriptor for evaluating the HER performance. More importantly, the ε_d value of −1.35 eV corresponding to the ΔG_{H*} close to zero can be utilized as a standard value to evaluate other transition-metal-based electrocatalysts using surface decoration strategies to optimize HER kinetics.

In brief, XPS and UPS reveal that the surface electronic structures of Mo_2C can be regulated by surface sulfur decoration, which is further confirmed by pDOS and ε_d calculations. To gain a comprehensive and more intuitive understanding of the surface charge redistribution, the charge density difference and electrostatic potential were investigated. Figure 4b illustrates the isosurface of charge density difference and the corresponding plane-averaged profile after sulfur decoration. It is evident that the electrons primarily accumulate around S atom as well as adjacent carbon atom and are diluted around the Mo atoms binding with S, in accordance with the XPS results. Surface charge redistribution will further regulate the electrostatic potential, thereby affecting the adsorption/desorption and diffusion of hydrogen intermediates. The plane-averaged potential of SSD-Mo_2C and P-Mo_2C are depicted in Figure 4d, in which the enlarged Φ confirms the UPS results. Furthermore, the introduction of surface sulfur decoration leads to a negative shift in the surface potential of Mo_2C, facilitating the adsorption of hydrogen protons. More importantly, an increased potential difference on the Mo_2C surface can be observed, as illustrated by the 2D slice mapping at a z coordinate of 12.8 Å, which corresponds to the average z coordinate of hydrogen intermediates. The surface S reduces the potential of adjacent active hollow sites, constructing an enhanced in-plane polarization field. Based on the results of ΔG_{H*}, the active hollow sites away from S atom are more readily occupied by hydrogen protons, under the influence of the in-plane polarization field, sufficient hydrogen protons will be delivered to the active hollow sites nearby S atoms for a more facile desorption reaction.[46] The possibility of hydrogen proton diffusion is further confirmed by transition state calculations, which show that the energy barrier for the diffusion process is significantly lower than that for direct desorption. In conclusion, the surface potential variation induced by surface sulfur decoration facilitates the adsorption and delivery of hydrogen protons, ensuring high hydrogen coverage as well as coordinated adsorption/desorption kinetics in SSD-Mo_2C.

Besides S, nitrogen (N) and phosphorus (P) are also widely used for electronic structure regulation of Mo_2C electrocatalysts. Therefore, detailed DFT calculations on the surface N/P decorated-Mo_2C were conducted as shown in Figure S18 (Supporting Information). First, the energy required for decorating N or P on the Mo_2C surface is higher than that for S, indicating that, in practice, decorating with N or P may not be as easy as with S. Second, surface phosphorus-decorated Mo_2C exhibits coordinated adsorption/desorption kinetics with a ΔG_{H*} close to zero at hydrogen coverages above 2/4. However, no improvement can be observed for surface nitrogen-decorated Mo_2C compared to P-Mo_2C. Finally, due to the P sites are widely recognized as highly active sites in molybdenum phosphide (MoP)-based HER electrocatalysts,[47] further investigation of the ΔG_{H*} for N, P, and S non-metal sites was performed. The P site exhibited significantly better hydrogen adsorption thermodynamics compared to N and S. Therefore, surface phosphorus decoration indeed represents a potential strategy for optimizing Mo_2C in HER, however, the optimization mechanism may be different from that of SSD-Mo_2C fundamentally.

Also, the sulfur modification strategy is widely used for optimizing HER electrocatalysts, especially Mo-based electrocatalysts, i.e., MoP,[48–50] molybdenum nitride (MoN),[51,52] molybdenum dioxide (MoO_2),[53–56] and molybdenum selenide ($MoSe_2$),[57–59] since the edge sites of MoS_2 are well-recognized as highly active centers for the HER reaction. Therefore, for an in-depth understanding of surface sulfur decoration on Mo-based materials, detailed DFT calculations on the ΔG_{H*} for various surface sulfur-decorated Mo-based electrocatalysts were performed as shown in Figure S20 (Supporting Information). Obviously, SSD-MoP and SSD-MoN exhibit significantly moderate ΔG_{H*}, indicating that the surface sulfur decoration strategy can effectively optimize the HER kinetics for MoP and MoN. This may be because Mo_2C, MoP, and MoN have similar hexagonal crystal systems and strong Mo—H bonds on the Mo-terminated surfaces. SSD-MoO_2 exhibits negligible optimization because MoO_2 itself lacks suitable active sites for HER. However, the good conductivity of MoO_2 makes it an ideal substrate for constructing MoS_2/MoO_2 heterostructures for highly efficient HER.[53,54] Similar to MoS_2, the edge sites of $MoSe_2$ are also highly active for the HER reaction. The edge sites of SSD-$MoSe_2$ exhibit more optimal ΔG_{H*} at low hydrogen coverages, which can increase the hydrogen coverage and facilitate the kinetics in the initial stage of HER. We believe these results will provide a comprehensive and in-depth perspective of surface sulfur decoration strategy for various Mo-based electrocatalysts and facilitate its application for other HER electrocatalysts.

3. Conclusion

A surface decoration strategy has been revealed to enhance the HER performances of Mo_2C by achieving coordinating adsorption/desorption kinetics, and the optimized SSD-Mo_2C exhibits the largest current density range with the desorption reaction as the rate-determining step, ultimately surpassing the commercial Pt/C electrocatalyst for high-efficiency hydrogen evolution. The high catalytic activity should be attributed to the surface charge redistribution induced by surface sulfur decoration, which subtly optimizes the ΔG_{H*} and enhances the in-plane polarization field, thereby facilitating the adsorption/desorption kinetics and delivery of hydrogen protons. Furthermore, this work demonstrates that coordinating adsorption/desorption kinetics provides an effective strategy to extend high current density growth rate range in HER.

4. Experimental Section

Synthesis of Cu_2O@CuS@PDA-Mo Nanocube Precursor: The Cu_2O@CuS@DPA-Mo nanocubes were synthesized according to the previous work with some modifications.[60] In brief, for the first step, 374.5 mg of $CuSO_4$•$5H_2O$ and 147 mg of $Na_3C_6H_8O_7\cdot 2H_2O$ were dissolved into 80 mL of deionized water. Subsequently, 20 mL of 1.25 м NaOH solution was added into the above solution and stirred for 15 min to obtain a suspension. Then, 50 mL of 0.03 м $C_6H_8O_6$ solution was added to the above suspension and stirred for an additional 3 min. The resulting orange mixture was aged for 1 h at ambient temperature. The precipitates, namely Cu_2O nanocubes, were collected by filtration and washed several times with water and ethanol. For the next step, 100 mg of the as-obtained Cu_2O nanocubes were dispersed in 60 mL of deionized water. Then, 40 mL of Na_2S aqueous solution (0.83 м, 0.2 mg mL^{-1}) was added to the Cu_2O nanocube dispersion and stirred for 2 min. The brown precipitates, namely Cu_2O@CuS nanocubes, were finally by filtration and washed several times with water and ethanol. For the last step, 100 mg of the as-prepared Cu_2O@CuS nanocubes, 50 mg of $C_8H_{12}ClNO_2$ (dopamine hydrochloride, DA), and 242 mg of Na_2MoO_4 were dissolved in 20 mL of deionized water. Then, 40 mL of ethanol was added to the above mixture solution. After stirring for 5 min, 0.3 mL of 28–30% $NH_3\cdot H_2O$ was quickly added to the mixture solution and stirring for another 2 h. The black precipitates, namely Cu_2O@CuS@PDA-Mo nanocubes, were collected by filtration and washed several times with water and ethanol.

Synthesis of SSD-Mo_2C Electrocatalyst: The SSD-Mo_2C electrocatalyst was synthesized through a process involving calcination followed by acidic etching. 100 mg of the as-obtained Cu_2O@CuS@PDA-Mo nanocubes were placed at the center of porcelain boats within a tube furnace and subjected to calcination at 800 °C for 2 h under an argon atmosphere. Then, hydrogen gas flow was introduced for an additional 20 min, followed by natural cooling. The resulting black powder was dispersed in a 0.1 м $FeCl_3$ aqueous solution, sonicated for 30 min, filtered, and washed several times with water and ethanol to remove any remaining inert Cu species.

Synthesis of P-Mo_2C Electrocatalyst: The preparation process was similar to that of SSD-Mo_2C, except that the precursor of Cu_2O@CuS@PDA-Mo was replaced with Cu_2O@PDA-Mo.

Synthesis of BSD-Mo_2C Electrocatalyst: The preparation process was similar to that of P-Mo_2C, except that the precursor of Cu_2O@PDA-Mo was replaced by Cu_2O@PPy-Mo-S. In brief, 100 mg of the as-prepared Cu_2O nanocubes, 200 µL of C_4H_4NH (pyrrole, Py), and 242 mg of Na_2MoO_4 were dissolved in 20 mL of deionized water. Then, 20 mL of $(NH_4)_2S_2O_8$ aqueous solution (0.025 м) was added to the above mixture solution and stirring for another 2 h. The black precipitates, namely Cu_2O@PPy-Mo-S nanocubes, were collected by filtration and washed several times with water and ethanol.

Synthesis of Mo_2C/MoS_x Electrocatalyst: The Mo_2C/MoS_x electrocatalyst was synthesized according to the previous work.[29] In brief, 100 mg of the as-prepared P-Mo_2C electrocatalyst was dispersed in 50 mL of deionized water containing 73.5 mg of thioacetamide. The solution was transferred into a Teflon-lined stainless-steel autoclave (100 mL) and heated at 200 °C for 10 h, respectively. After cooling, the product was collected by filtration and washed with water and ethanol for several times.

Characterizations: XRD analysis was conducted using a D/max 2500 system with a Cu Kα radiation source. Morphology and microstructures were observed using a Zeiss Sigma 300 scanning electron microscope scanning electron microscope and a FEI Tecnai F20 transmission electron microscope. The surface elemental compositions were determined using XPS (Thermo Fisher Scientific K-ALPHA), and the valence bands were analyzed using UPS (Kratos Axis Ultra HAS with a He (I) photo line of 21.22 eV). EPR spectra were obtained using a Bruker EMX PLUS spectrometer at the frequency of 9.411 GHz at 100K. Raman spectra were measured using a Raman microscope (LabRam HR Evolution) with 532 nm wavelength laser sources. The Zeta potential measurements were conducted with a dynamic light scattering system (Malvern Zetasizer Nano ZS90).

Supporting Information

Supporting Information is available from the Wiley Online Library or from the author.

Acknowledgements

Financial support from the National Natural Science Foundation of China (Grant No. 52374407) is gratefully acknowledged.

Conflict of Interest

The authors declare no conflict of interest.

Data Availability Statement

The data that support the findings of this study are available from the corresponding author upon reasonable request.

Keywords

electrocatalysts, hydrogen evolution reaction, molybdenum carbides, surface decoration

Received: April 30, 2024
Revised: June 5, 2024
Published online:

---

[1] M. Dresselhaus, I. Thomas, *Nature.* **2001**, *414*, 332.
[2] H. Gray, *Nat. Chem.* **2009**, *1*, 7.
[3] T. Shinagawa, A. Garcia-Esparza, K. Takanabe, *Sci. Rep.* **2015**, *5*, 13801.
[4] Y. Chen, R. Ding, J. Li, J. Liu, *Appl. Catal. B.* **2022**, *301*, 120830.
[5] C. Zhang, Q. Liu, P. Wang, J. Zhu, D. Chen, Y. Yang, Y. Zhao, Z. Pu, S. Mu, *Small.* **2021**, 2104241.
[6] S. Roy, D. Bagchi, L. Dheer, S. Sarma, V. Rajaji, C. Narayana, U. Waghmare, S. Peter, *Appl. Catal. B.* **2021**, *298*, 120560.
[7] H. Yan, Y. Xie, Y. Jiao, A. Wu, C. Tian, X. Zhang, L. Wang, H. Fu, *Adv. Mater.* **2018**, *30*, 1704156.
[8] D. Vikraman, S. Hussain, K. Karuppasamy, A. Feroze, A. Kathalingam, A. Sanmugam, S. Chun, J. Jung, H. Kim, *Appl. Catal. B.* **2020**, *264*, 118531.
[9] X. Zang, W. Chen, X. Zou, J. N. Hohman, L. Yang, B. Li, M. Wei, C. Zhu, J. Liang, M. Sanghadasa, J. Gu, L. Lin, *Adv. Mater.* **2018**, *30*, 1805188.
[10] Y. Liu, G. Yu, G. Li, Y. Sun, T. Asefa, W. Chen, X. Zou, *Angew. Chem., Int. Ed.* **2015**, *54*, 10752.
[11] Y. Lu, C. Yue, Y. Li, W. Bao, X. Guo, W. Yang, Z. Liu, P. Jiang, W. Yan, S. Liu, Y. Pan, Y. Liu, *Appl. Catal. B.* **2021**, *296*, 120336.
[12] Y. Chen, Y. Zhang, W. Jiang, X. Zhang, Z. Dai, L. Wan, J.-S. Hu, *ACS Nano.* **2016**, *10*, 8851.
[13] F. Ma, H. Wu, B. Xia, C. Xu, X. Lou, *Angew. Chem., Int. Ed.* **2015**, *54*, 15395.
[14] X. Lu, L. Yu, J. Zhang, X. (David) Lou, *Adv. Mater.* **2019**, 1900699.
[15] T. Gu, R. Sa, L. Zhang, D. Li, R. Wang, *Appl. Catal. B.* **2021**, *296*, 120360.
[16] L. Zhao, H. Yuan, D. Sun, J. Jia, J. Yu, X. Zhang, X. Liu, H. Liu, W. Zhou, *Nano Energy.* **2020**, *77*, 105056.
[17] J. Wan, J. Wu, X. Gao, T. Li, Z. Hu, H. Yu, L. Huang, *Adv. Funct. Mater.* **2017**, *27*, 1703933.
[18] T. Gu, R. Sa, L. Zhang, F. Zhou, R. Wang, X. Li, *J. Mater. Chem. A* **2020**, *8*, 20429.
[19] Y. Ma, M. Chen, H. Geng, H. Dong, P. Wu, X. Li, G. Guan, T. Wang, *Adv. Funct. Mater.* **2020**, *30*, 2000561.
[20] H. Chen, L. Yang, R. Wang, W. Zhang, R. Liu, Y. Yun, N. Wang, S. Ramakrishna, L. Jiao, Y. Long, *Small.* **2023**, *19*, 2304086.
[21] J. Li, J. Hu, M. Zhang, W. Gou, S. Zhang, Z. Chen, Y. Qu, Y. Ma, *Nat. Commun.* **2021**, *12*, 3502.
[22] Z. Lin, Z. Wang, J. Gong, T. Jin, S. Shen, Q. Zhang, J. Wang, W. Zhong, *Adv. Funct. Mater.* **2023**, *33*, 2307510.
[23] S. Pan, C. Li, T. Xiong, Y. Xie, F. Luo, Z. Yang, *Appl. Catal. B.* **2024**, *341*, 123275.
[24] T. Chao, W. Xie, Y. Hu, G. Yu, T. Zhao, C. Chen, Z. Zhang, X. Hong, H. Jin, D. Wang, W. Chen, X. Li, P. Hu, Y. Li, *Energy Environ. Sci.* **2024**, *17*, 1397.
[25] R. Tang, Y. Yang, Y. Zhou, X. Yu, *Adv. Funct. Mater.* **2024**, *34*, 2301925.
[26] C. Tsai, H. Li, S. Park, J. Park, H. S. Han, J. K. Nørskov, X. Zheng, F. Abild-Pedersen, *Nat. Commun.* **2017**, *8*, 15113.
[27] X. Wang, Y. Zhang, H. Si, Q. Zhang, J. Wu, L. Gao, X. Wei, Y. Sun, Q. Liao, Z. Zhang, K. Ammarah, L. Gu, Z. Kang, Y. Zhang, *J. Am. Chem. Soc.* **2020**, *142*, 4298.
[28] C. Tsai, H. Li, S. Park, J. Park, H. S. Han, J. K. Nørskov, X. Zheng, F. Abild-Pedersen, *Nat. Commun.* **2017**, *8*, 15113.
[29] C. Tang, W. Wang, A. Sun, C. Qi, D. Zhang, Z. Wu, D. Wang, *ACS Catal.* **2015**, *5*, 6956.
[30] J. Xiong, J. Li, J. Shi, X. Zhang, N. Suen, Z. Liu, Y. Huang, G. Xu, W. Cai, X. Lei, L. Feng, Z. Yang, L. Huang, H. Cheng, *ACS Energy Lett.* **2018**, *3*, 341.
[31] C. Lu, D. Tranca, J. Zhang, F. Rodrıguez Hernández, Y. Su, X. Zhuang, F. Zhang, G. Seifert, X. Feng, *ACS Nano.* **2017**, *11*, 3933.
[32] C. Lv, Z. Huang, Q. Yang, G. Wei, Z. Chen, M. G. Humphrey, C. Zhang, *J. Mater. Chem. A.* **2017**, *5*, 22805.
[33] X. Ren, J. Zhao, Q. Wei, Y. Ma, H. Guo, Q. Liu, Y. Wang, G. Cui, A. M. Asiri, B. Li, B. Tang, X. Sun, *ACS Cent. Sci.* **2019**, *5*, 116.
[34] P. Zhang, Y. Liu, T. Liang, E. H. Ang, X. Zhang, F. Ma, Z. Dai, *Appl. Catal. B.* **2021**, *284*, 119738.
[35] L. Zhai, X. She, L. Zhuang, Y. Li, R. Ding, X. Guo, Y. Zhang, Y. Zhu, K. Xu, H. J. Fan, S. P. Lau, *Angew. Chem., Int. Ed.* **2022**, *61*, 202116057.
[36] P. D. Tran, T. V. Tran, M. Orio, S. Torelli, Q. D. Truong, K. Nayuki, Y. Sasaki, S. Y. Chiam, R. Yi, I. Honma, J. Barber, V. Artero, *Nat. Mater.* **2016**, *15*, 640.
[37] W. Fu, Y. Wang, W. Tian, H. Zhang, J. Li, S. Wang, Y. Wang, *Angew. Chem., Int. Ed.* **2020**, *59*, 23791.
[38] J. Huang, Y. Liu, L. Wang, Z. Hou, Z. Zhang, X. Zhang, J. Liu, *Chem. Eng. J.* **2023**, *469*, 143908.
[39] K. Kimbulapitiya, B. Rehman, S. Wani, C. Chen, R. Cyu, A. Manikandan, M. Date, Y. Peng, R. Kumara, F. Chuang, Y. Chueh, *Nano Energy.* **2024**, *122*, 109235.
[40] A. Huang, H. Huang, F. Wang, N. Ke, C. Tan, L. Hao, X. Xu, Y. Xian, S. Agathopoulos, *Small.* **2024**, *20*, 2308068.
[41] W. Liu, X. Wang, J. Qu, X. Liu, Z. Zhang, Y. Guo, H. Yin, D. Wang, *Appl. Catal. B.* **2022**, *307*, 121201.
[42] W. Spychalski, M. Pisarek, R. Szoszkiewicz, *J. Phys. Chem. C.* **2017**, *121*, 26027.

[43] N. Zhang, A. Jalil, D. Wu, S. Chen, Y. Liu, C. Gao, W. Ye, Z. Qi, H. Ju, C. Wang, X. Wu, L. Song, J. Zhu, Y. Xiong, *J. Am. Chem. Soc.* **2018**, *140*, 9434.
[44] J. Kibsgaard, T. Jaramillo, F. Besenbacher, *Nat. Chem.* **2014**, *6*, 248.
[45] J. Nørskov, T. Bligaard, J. Rossmeisl, C. Christensen, *Nat. Chem.* **2009**, *1*, 37.
[46] Y. Liu, Y. Chen, Y. Tian, T. Sakthivel, H. Liu, S. Guo, H. Zeng, Z. Dai, *Adv. Mater.* **2022**, *34*, 2203615.
[47] P. Xiao, M. A. Sk, L. Thia, X. Ge, R. J. Lim, J.-Y. Wang, K. H. Lim, X. Wang, *Energy Environ. Sci.* **2014**, *7*, 2624.
[48] Q. Liu, Z. Xue, B. Jia, Q. Liu, K. Liu, Y. Lin, M. Liu, Y. Li, G. Li, *Small.* **2020**, *16*, 2002482.
[49] K. Liang, S. Pakhira, Z. Yang, A. Nijamudheen, L. Ju, M. Wang, C. I. Aguirre-Velez, G. E. Sterbinsky, Y. Du, Z. Feng, J. L. Mendoza-Cortes, Y. Yang, *ACS Catal.* **2019**, *9*, 651.
[50] Y. Huang, X. Song, J. Deng, C. Zha, W. Huang, Y. Wu, Y. Li, *Appl. Catal. B.* **2019**, *245*, 656.
[51] J. Tan, Y. Mei, H. Shen, H. Liu, T. Azhagan, W. Song, T. Thomas, J. Liu, M. Yang, M. Gao, *ChemCatChem.* **2020**, *12*, 122.
[52] J. Chen, X. Liu, H. Wang, C.-L. Chiang, P. Hou, J. Li, H. Jin, S. Liu, X. Meng, Y.-G. Lin, J.-M. Lee, Q. Zhao, *Chem. Eng. J.* **2023**, *466*, 143221.
[53] X. Yu, F. Yan, Y. Zhao, B. Geng, X. Ma, L. Wu, X. Zhang, Y. Chen, *Appl. Catal. B.* **2024**, *343*, 123534.
[54] F. Gong, M. Liu, S. Ye, L. Gong, G. Zeng, L. Xu, X. Zhang, Y. Zhang, L. Zhou, S. Fang, J. Liu, *Adv. Funct. Mater.* **2021**, *31*, 2101715.
[55] S. Geng, Y. Liu, Y. S. Yu, W. Yang, H. Li, *Nano Res.* **2020**, *13*, 121.
[56] J. Liu, B. Gao, W. Qin, J. Jiang, M. Li, C. Wei, Q. Xu, *ACS Appl. Energy Mater.* **2022**, *5*, 10483.
[57] J. Yang, Y. Liu, C. Shi, J. Zhu, X. Yang, S. Liu, L. Li, Z. Xu, C. Zhang, T. Liu, A. C. S. Appl, *Energy Mater.* **2018**, *1*, 7035.
[58] S. Li, W. Zang, X. Liu, S. J. Pennycook, Z. Kou, C. Yang, C. Guan, J. Wang, *Chem. Eng. J.* **2019**, *359*, 1419.
[59] X. Wang, C. Xue, N. Kong, Z. Wu, J. Zhang, X. Wang, R. Zhou, H. Lin, Y. Li, D.-S. Li, T. Wu, *Inorg. Chem.* **2019**, *58*, 12415.
[60] Y. Fang, D. Luan, Y. Chen, S. Gao, X. W. Lou, *Angew. Chem., Int. Ed.* **2020**, *59*, 7178.